sciendo

Research Note • DOI: 10.2478/gsr-2023-0002 GSR • 12 • 2024 • 1–17

Gravitational and Space Research

The Magnitude of the Soret Force on Colloidal Particles Measured in Microgravity

Matthew L. Lynch[1]*, Thomas E. Kodger[2], Paolo Palacio-Mancheno[1], Mark W. Pestak[3], William V. Meyer[4]

[1]Corporate Research Division, The Procter & Gamble Company, 8700 Mason Montgomery Rd, Mason, OH, USA 45040; [2]Physical Chemistry and Soft Matter, Wageningen University & Research, Stippeneng 4, 6708 WE, Wageningen, NL; [3]Space Engineering Division, KBR Wyle Technology Services, 6745 Engle Rd, Suite 105, Cleveland, OH, USA 44130; [4]Universities Space Research Association (USRA) with GEARS (Glenn Engineering and Research Support), NASA Glenn Research Center, 2001 Aerospace Parkway, MS HX5-2, Brook Park, OH, USA 44152

Abstract

There is a broad interest in both industry and academe in understanding the time-evolution in the microstructure of colloidal gels, as such changes affect the properties of the gels including product self-life and rheology. In colloidal gels, the time-evolution results from the magnitude and the relative proportions of forces—including gravity, acting on the colloidal particles. The aim of this study was to measure the magnitude of the Soret force acting on the colloidal particles in a model gel in the microgravity on the International Space Station, as a proxy for gravitational forces in Earth-based experiments. It was found that the Soret force could be used to create an effective gravitational force of between about 10 x 10^{-17} N (3 milli-G) and 3 x 10^{-17} N (1 milli-G) on the colloidal particles, where the lower limit is set by the dominance of particle flux from Brownian forces. These results should allow mapping the behavior of colloidal gels broadly described in literature on other gels—such as polymer gels of industrial interest, where the colloidal particles are much smaller.

Keywords

Soret Effect • Microgravity • Colloidal Particles • Gels • International Space Station

Introduction

The overarching goal of this research is to measure the time-dependent effects of Brownian and non-Brownian forces on aggregated colloidal dispersions, with the goal of mapping the structural evolution of colloidal gels onto other gel systems. Such models are of both fundamental academic importance and crucial to fuel the development of consumer and other products comprising complex fluids. The approach taken has been to measure the magnitude of the Soret force as a proxy for the gravitational force in a microgravity environment, which would enable the measurement of the magnitude and ratio of stresses applied on the colloidal gel system and which would enable mapping the behavior of colloidal gels onto the behavior of “clumpy” polymer gels. Any conclusions should be broadly applicable to other colloidal gel systems.

Gels are the focus of fundamental research because of the properties they impart on systems of industrial interest. Gels are found in a wide range of industrial systems including in food (Genovese et al., 2007; Dickinson, 2015), medicines (Ashley et al., 2013), and consumer products (Wagner and Brady, 2009; Solomon and Spicer, 2010). One system of particular interest is a blend of two polysaccharides that can be used as a suspension gel with a yield stress to enable novel sprayable products. The system is composed of a binary mixture of polymer “particles” that are designed to withstand the stress applied from the buoyancy of dispersed capsules (Lynch et al., 2018) and drops (Lynch et al., 2020). The gel breaks as it flows into colloidal scale domains (Lin et al., 2020). In each case, it remains of acute interest to connect the microstructure to the short-term and long-term properties of the gels. In this important system, this mapping is extraordinarily valuable as it allows access to the learnings of a large body of literature that does not exist for the polymer system and allows the direct visualization of the primary particles, which are vanishingly small on the order of 100 nm.

Colloidal gels represent a large body of research for which microstructure-property relationships have been explored (Lu and Weitz, 2013; Suman and Wagner, 2022). Colloidal gels are generally composed of a dispersion of micron-sized particles—often spherical, which exhibit a net attractive potential, and which aggregate into space-spanning networks with a complex topology and connectivity (Dinsmore and Weitz, 2002; Dinsmore et al., 2006; Gao et al., 2015). The microstructure and properties of the

†Corresponding author: Matthew L. Lynch
E-mail: lynch.ml@pg.com

colloidal gels are governed by the effect of the combination of at least four different forces: hydrodynamic, Brownian, gravitational, and particle-particle forces (Russel et al., 1999). The hydrodynamic forces result from the interaction of moving particles with the solvent, often attributed to both retardation of the movement of primary particles, and the bulk movement of particle and particle aggregates in flow. Brownian forces arise from the stochastic nature of the solvent interactions with particles resulting in random walk of the particles, and often attributed to the formation, aging, and rheology of gels. Gravitational force is a body force, and in most systems it is in the direction of the gravitation field with a magnitude proportional to the density difference between the particles and solvent. In ground-based experiments, gravity is nulled—with only short-term success, by density-matching particles with the surrounding solvent. However, it is extraordinarily difficult to precisely control with slight temperature changes upsetting the balance. Gravity also results in delayed effects on colloidal gels (Padmanabhan and Zia, 2018). Experiments in microgravity effectively null gravitational forces. Particle–particle forces take several forms including electrostatic, Derjaguin-Landau-Verwey-Overbeek (DLVO), polymer bridging and/or depletion forces. Depletion forces are particularly leveraged in this work arising in a way often described from the imbalance of the osmotic pressure from non-absorbing polymers dissolved in the solvent excluded from the region between bonded particles. Depletion force are tunable in magnitude, shape, and distance (Dibble et al., 2006; Lu et al., 2008), making it ideal in this work for creating weak, ergodic gels. The experimental system contains an uneven concentration of particles at different spots in the volume, allowing Soret measurements in low-density regions in the cells with the ability to translate the measurement to regions in the cell with high-density.

Some of the common rheological behaviors between colloidal gels and clumpy polymer systems suggest a common link between forces and the ratio of forces that enable mapping. It has been long understood that there are links between gel microstructure and rheology (Rueb and Zukoski, 1997; Johnson et al., 2019). One particularly intriguing rheology behavior is referred to as an “Avalanche” behavior, observed in numerous colloidal systems (Coussot et al., 2002). This is a creep experiment in which a constant stress is applied to the gel, and the gel responds with a time-dependent strain deformation potentially in three regimes: (1) the creep regime, (2) the rheological yield regime, and (3) the post yield flow regime. The Avalanche behavior was modeled by Landrum (Landrum et al., 2016) for colloidal gels. The Avalanche behavior for the polymer gel is quantitatively the same and shown in Figure 1a. and the resulting incubation time is shown in Figure 1b. The paper by Landrum also connects the different behaviors to the magnitude and ratio

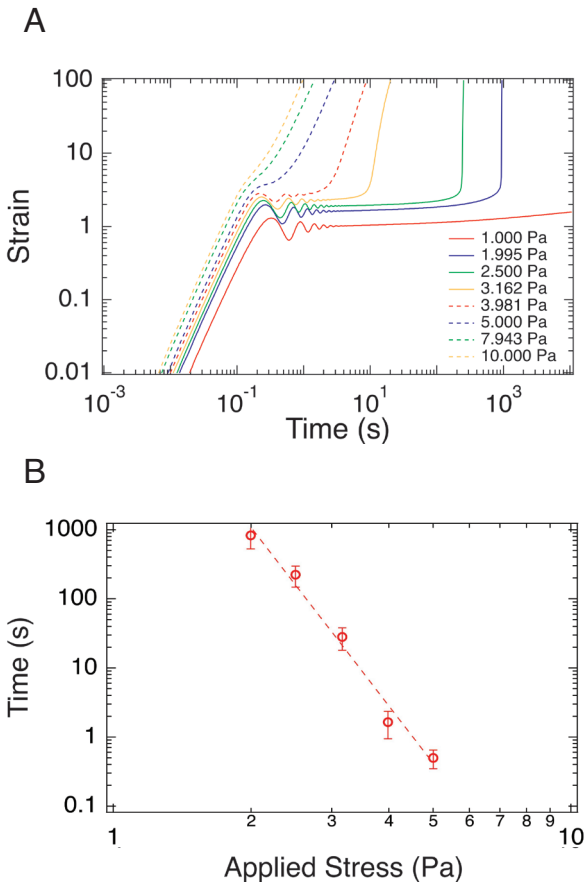

Figure 1. The rheological behavior of the XK gum polymer gel system described in Lynch et al. (2018) and Lynch et al. (2020). **(A)** The creep flow behavior with different applied stresses. With low applied stress (1.000 Pa, red), the gel strains but exhibits no fluid-like flow at long times; however, at high applied stress (2.500 Pa, green), the gel strains and eventually breaks resulting in viscous flow at long times. **(B)** The gel breakage follows a power-law behavior with applied stress and time. This is the same rheological behavior in colloidal gels described in Landrum et al. (2016) and more broadly described in Coussot et al. (2002).

of these fundamental forces. In total, these sources provide evidence that it is possible to reduce the complexity of the polysaccharide systems with the richness understood in colloidal gels. However, the challenge is how to find regions in the colloidal system in which the magnitude and ratio of these fundamental forces overlap with the polymer system, but which can be difficult as colloidal particles are orders of magnitude different than polymer particles, requiring fine-tuning of gravitational forces without significantly changing compositions. Within here lies the opportunity of leveraging Soret forces in microgravity as a proxy for gravitational forces. Colloidal systems have been extensively measured in

microgravity, with a range of interparticle interactions. Much of the early work focused on the behavior of dispersions of colloidal spheres sporting only hard-sphere interactions including crystallization in microgravity driven by entropy alone (Zhu et al., 1997) and development of phase diagrams of hard spheres, showing different phase domains and domains with growth habits (Cheng et al., 2001). Later work focused on behavior of aggregating dispersions of colloidal spheres in which aggregation was forced by electrostatic interactions by the inclusion of salt (Manley et al., 2004). Further studies focused on aggregation of dispersions of colloidal spheres induced by depletion interactions, resulting from the addition of non-absorbing polymer. Much of this work focused on phase separation through spinodal decomposition (Bailey et al., 2007), and cases in which the phase separation was arrested during the spinodal decomposition process to form gels (Sabin et al., 2012). Other work focused on the aggregation of spheres in microgravity using Casimir forces (Veen et al., 2012). More recent work has focused on the application of external fields to drive mechanical deformation of aggregated spheres (Swan et al., 2014), including multiscale kinetics (Swan et al., 2012). This body of work instructs the studies here within.

The Soret force—often described as the thermophoretic force—results in the movement of particles along a temperature gradient, in a way to suggest that it could be used as a proxy for a “tunable” gravitational force on the particles in microgravity. Although the exact origin of Soret force is the subject of debate (Duhr, 2006; Platten, 2006; Kohler and Morozov, 2016), many suggest that it originates from imbalanced interactions of solvent molecules with the surface of particles. The effect is to create movement of particles in a temperature gradient, such that the drift velocity scales as $v=-D_t \cdot \nabla T$, where D_t is the thermophoretic coefficient. The magnitude of the Soret force can be tuned in a microgravity environment by adjusting the temperature gradient, without changing any chemistry in the mixtures. Further, in the limit where the temperature gradient is constant over a volume, it is anticipated the Soret force can be used as proxy for a “tunable” gravitational force on the particles in microgravity. There are number of published papers of the Soret force, which we use to design the experiments described in this paper. Van Vaerenbergh and Legros did some initial work on Soret effects in microgravity on the molecules of organic solvents (Van Vaerenbergh and Legros, 1998). Putnam et al. demonstrated that magnitude and sign of the Soret force for charge 26-nm polystyrene spheres varies with type and amount of added salt, although they acknowledge that there is no good theory to underscore these dependencies (Putnam et al., 2007). Duhr and Braun demonstrated the Soret force with 200-nm size polystyrene spheres over a range of concentrations, but also that the magnitude of the effect tracks the linear relationship only within small temperature gradients (Duhr and Braun, 2006). Ning et al. demonstrated that interacting silica colloidal particles change the magnitude of the thermophoretic coefficient as a consequent of particle aggregation (Ning et al., 2006). Putnam et al. illustrated the thermophoretic effects on 2-nm diameter nanoparticles and lysozyme molecules, importantly demonstrating the dependence on the average absolute temperature (Putnam et al., 2007). Vigolo et al. revealed the thermophoretic effects on microemulsion drops, and that the magnitude of the effects is not dependent on the size of the drops (Vigolo et al., 2007). Braibanti et al. shared the same basic results, but for polystyrene sphere (Braibanti et al., 2008). These results are built into the specifics experimental design here within.

In this work, the magnitude of the Soret force is measured in a microgravity on the International Space Station (ISS) on particles in an ergodic colloidal dispersion and expressed as an equivalent gravitational force. The magnitude of the force is tuned by adjustment of the temperature gradient in the cell. With each adjustment, the distribution of particles is allowed to equilibrate in response to the applied temperature gradient. The distribution is modeled as a system of Brownian particles in a gravitational field, which eliminates the need for particle tracking, eliminates the need to consider hydrodynamic flow, and removes temporal fluctuations in particle positions over an experiment. This allows the description of the Soret force in terms of an equivalent gravitational force. This is all done in a dilute part of the sample where results can be modeled from largely unbounded particles. It is found that the Soret force is tunable and on the order of milli-G, allowing the potential to map measured microstructures in this colloidal system onto the desired polymer system by access magnitude and relative magnitudes of stresses in the system. Future work will focus on applying these learnings to measure in volumes in the cell from largely bound particles

Material and Methods

Sample Preparation

The samples were composed of weakly-attractive colloidal particles dispersed in a mixture of solvent and non-absorbing polymer. The particles were colloidal spheres prepared from a copolymer mixture of 22% trifluoroethyl methacrylate (poly-TFEMA) (Aldrich) and 78% tert-butyl methacrylate (Poly-TBMA) (Aldrich) through free radical dispersion polymerization (Kodger et al., 2015; Kodger et al., 2017). Two batches were prepared: one batch consisted of 1.92 ± 0.31 um-diameter spheres labeled with pyrromethene 605 (emission: 545nm, excitation: 605nm), and one batch consisted of 1.59 ± 0.19 um-diameter spheres labeled with pyrromethene 546 (emission:

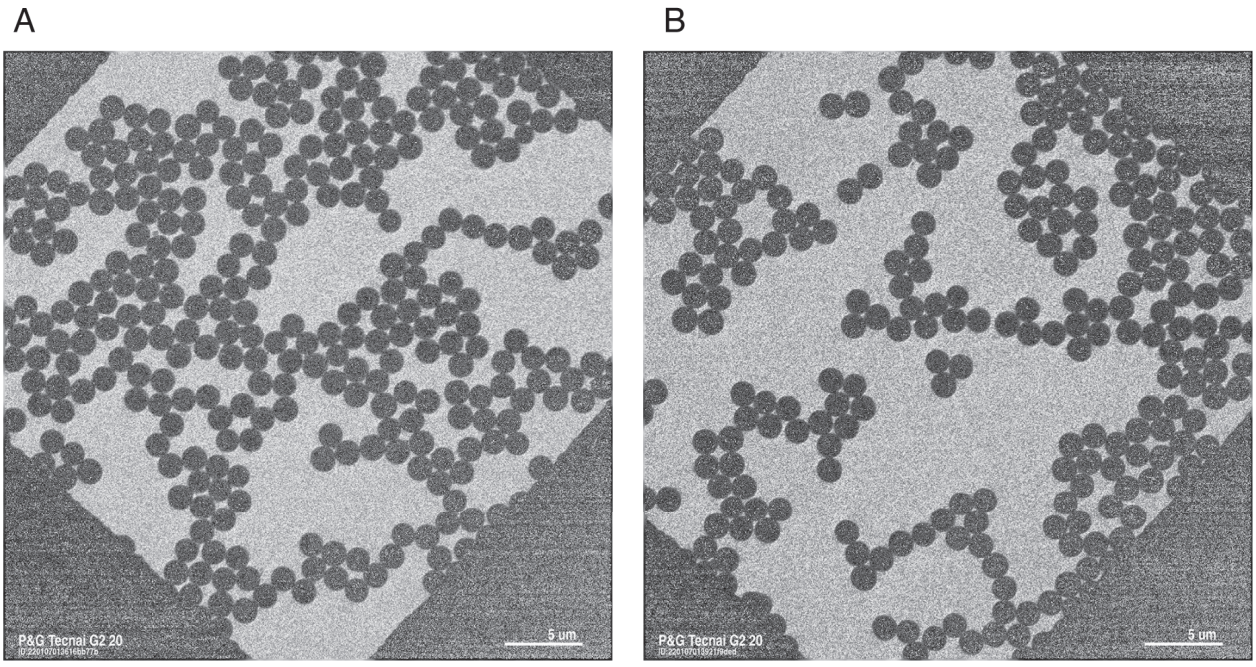

Figure 2. Electron micrographs of the colloidal particles used in these experiments. **(A)** The larger particles were measured 1.92 ± 0.31 um in diameter. **(B)** The smaller particles were measured 1.59 ± 0.19 um in diameter.

488nm, excitation: 515nm). The sizes and mono-dispersity of each batch were determined with electron microscopy (Figure 2) using the Circle Hough Transform. Each particle was dispersed at 2.5 volume fraction (to reflect the amount of each particle in the polymer gel) in a mixture of solvent and non-absorbing polymer. The solvent was composed of 27 v/v% sulfolane and 73 v/v% formamide, chosen to match the refractive index and density of the colloidal particles, allowing the measurement of the distribution of particles to depths of 70 um into the sample with confocal microscopy. Next, 10 mM sodium chloride was added to the solvent to screen electrostatic interactions between the dispersed particles. Then, 1M Da molecular weight poly (sodium 4-styrene sulfonate) (Sigma-Aldrich) was dissolved in the solvent at a concentration of 0.9 mg/mL, to induce a depletion force of about 1 kT between the particles (Asakura and Oosawa, 1954), estimated by light-scattering measurements to determine the radius of gyration Rg, osmotic pressure, and depletion volume between the particles. This ensured an ergodic sample, with some aggregation. The measured concentration of the particles in the measured science spot depended on sample mixing.

Hardware

The hardware in the microscope is shown in Figure 3A. The samples were contained in a cuboid borosilicate VitroCom glass capillary cell (product #3520) with external dimensions of 50,000 um x 2,286 um x 486 um and with a chamber with internal dimensions of 44,000 um x 2,000 um x 200 um centered in the capillary (Figure 3B). The sample was wicked into one end of the cell, a magnetic stirring bar (wire) was inserted, and both ends of the cell were sealed with epoxy.

The glass capillary cell was mounted on a thermal bridge heater to control temperature in the cell (Figure 3C). The thermal bridge heater (ZIN Technologies, part number S2092MD20003B) was constructed from single, flat piece of copper resembling the cross-section of an I-beam, with a narrow strip with two square sections on the end of the thermal bridge. The cell was mounted to the top of the thermal bridge along its complete length with a thermal epoxy (Master Bond: EP42HT-2AO-1BLACK). Two Peltier thermoelectric modules (TEM1 and TEM2) were affixed to the two square sections at the end, which can be independently controlled through the wire connections. In these measurements, TEM1 and TEM2 were always set to the same temperature. Five micro NTC thermistors (QTI, E321/T321) were equally spaced along the length of the thermal bridge to measure temperature over the length of the cell.

The cell and thermal bridge assembly was mounted inside a magnetic controller (Figure 3D), to enable mixing along the sample volume. The magnetic controller was a set of twenty-two electromagnets—half placed on one side of the cell and half placed on the other side of the cell. The electromagnets were controlled to translate and rotate of the magnetic stirring bar through the sample volume in the cell. The samples

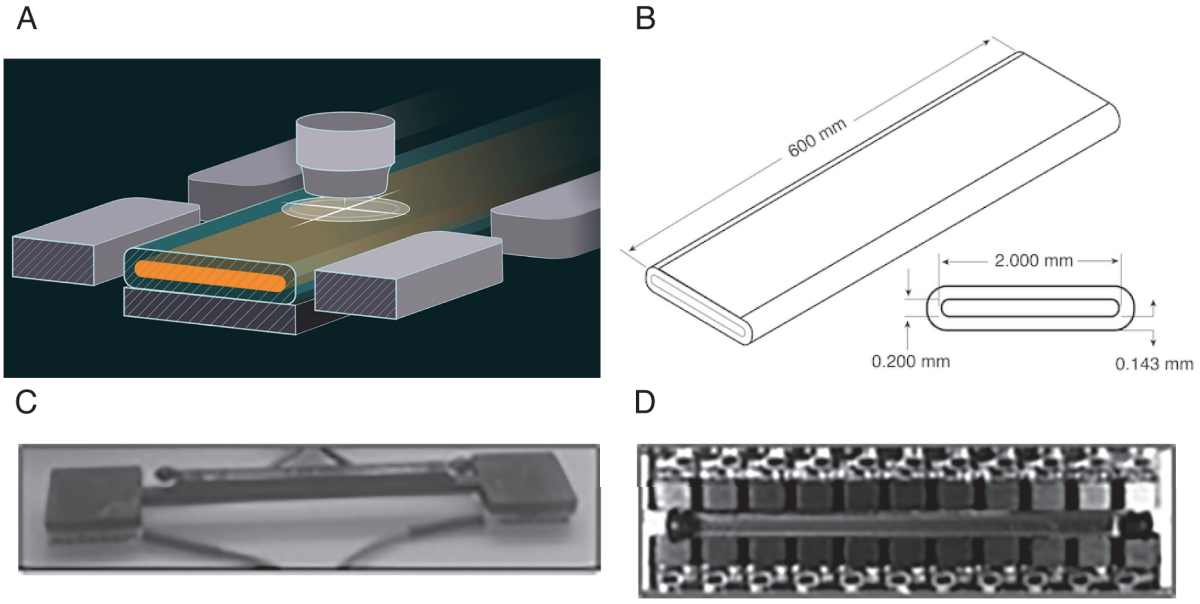

Figure 3. The experimental hardware used in these experiments. **(A)** An edge-on drawing of the showing the glass capillary cell (center) with sample chamber (orange), the thermal bridge (bottom), several of the electromagnets (left, right), and the confocal objective (top). **(B)** Sketch of the borosilicate VitroCom glass capillary cell. **(C)** Image of the glass capillary cell mounted on the thermal bridge, with the two thermoelectric heaters mounted at each end. **(D)** Top-view showing the glass capillary cell and thermal bridge mounted in a bank of electromagnets.

were mixed by moving the stirring bar over the length of the sample for 1 hour. This process should result in complete and homogeneous randomization of the sample. However, in practice, this was not the result, as particles often aggregated at the end of the cell and the volume often contained a small pocket of air. For this reason, after mixing, the sample was inspected with a low magnification 10X objective to choose a location for the measurement. It was common, and often by design, that the science spot had a different volume fraction of particles than otherwise anticipated from the preparation of the sample. In this work, the science spot was chosen to be lower volume fractions to minimize the fraction of bounded particles at the start of the measurement.

Three hardware configurations were mounted side-by-side in the Sample Module Assembly. The Sample Module Assembly attached to the microscope stage, allowing movement of the samples in the x-, y-, and z-direction, where the x-direction is along the long axis of the capillary, the y-direction is orthogonal to the x-direction in the same plane of the capillary, and the z-direction is orthogonal to both these directions in a right-hand coordinate system with the positive direction into the sample from the objective. The top of the cells was exposed allow imaging with a contact (63X oil) immersion or a non-contact objective (10X air). In the case of the former, a small drop of oil is placed on the cell, which can be moved to the point of measurements.

Confocal Microscope

The Light Microscopy Module was a modified commercial, highly flexible light-imaging confocal microscope facility that provides researchers with diagnostic hardware and software that can be commanded to run scripts onboard the ISS. The microscope were a modified (motorized) Leica DM-RXA, which uses an excitation doubled-YAG laser (532 nm) with an output power adjustable from 0 to 60 mw, a Yokogawa CSU-X1-M1 confocal unit (basic model), FB1 collimating lens, a Yokogawa C-103 camera adapter, and IMPERX Bobcat B2020 (GigE Vision) camera. Three different objectives were used in these experiments: 2.5X air objective, 10X air objective, and 63X oil-immersion objective. The first objective was used to look for large features, such as bubbles, along the length of the cell; the second objective was used to check the dispersion of particles after mixing and to find the best science spot after mixing; and the third objective was used to image the particles in the volume at the science location in the measurement of the Soret force. The original intent was to use two different dyes distinguish between the two size colloidal particles, but this proved impossible in practice.

Experiment

After mixing, the low magnification objectives were used to find an appropriate science spot. The science spot was selected to contain well-dispersed particles, often at a volume

fraction less than 5 v%/v%. The temperature was set with the thermoelectric modules (TEM1 and TEM2). A small spot of immersion oil was placed on the top of the cell, and the 63X objective was put into place. Image stacks were collected over the course of the experiment. One image stack consisted of fifty images, where each image (or slice) had dimensions of 1824 pixels wide (x-direction) and 1340 pixels tall (y-direction) at a resolution of 0.095 um/pixel in each direction, and a stack comprised fifty such images equally spaced at 1.4 um in the science volume. The first image was collected in the volume adjacent to the objective (by convention, z = 0), with the other image collected by rastering into the volume. This results in a science volume of about a 173-um x 127-um x 70-um. In this design, each image was collected in about 0.5 seconds, each stack collected in about 25 seconds with about 30 seconds between the start of one stack and the subsequent stack. Each image was stored as an 8-bit grayscale .tiff file (in displayed images, the x-direction and y-direction were set by the convention of the image, with the position z-direction being captured in the image below).

Determining Particle Positions

Images were imported as “raw data” into Avizo (Avizo Lite V9.2.0, FEI, Thermo Fisher Scientific). First, the “raw data” captured in each image were digitally filtered in two steps and then segmented to create new images containing “enhanced data.” First, an intensity threshold of 70 was applied to the “raw data” image; this threshold was set to the grayscale value of the minimum of the image histogram such that it separates the foreground, particles in the imaging place, and removes the background, a diffuse signal from particles not in the focal plane of the “raw data” image. The image was further cleaned by comparing the resulting image with the “raw data” image, removing any small unconnected features, thereby removing random noise and artifacts, resulting in “clean data.” Second, the “clean data” was passed through two filters: a Gaussian filter and a connected components analysis filter. The Gaussian filter intensifies the local maxima of each particle, improving object identification. The connected components analysis filter excludes low-intensity particles and excessively bright agglomerations, resulting in “enhanced data.” Third, the “enhanced data” was transformed into “binary data” for the material statistics analysis. From the “binary data” for the 3D stack, it was possible to make a count of the number of voxels contained in an object, the volume of the object, and the centroid location of the object.

To ensure the accuracy of the Avizo algorithms in determining the z-position of the particles, the outcome from this procedure was compared with manual centroid determinations from the “raw data.” The question here: the particles were 2 ums. The resolution in the x-direction and y-direction of the image was much less than 2 ums, and the expectation of precision in these directions is certain. However, the resolution in the z-direction was much less. The balance in 1.4 um step means that at best, we slice the imaging only through particle twice. However, the fluorescence of the particle—as measured by the microscope—had a significant partial volume effect that carries into the volume above and below a particle in the z-direction (Figure 4). This means that the microscope saw images of the particle some distance micrometers above and below the image. In concept, we can measure the intensity of the fluorescence above and below the particle at these different points and extrapolate to the maximum value of indication of the z-direction position. This value was compared back to that extracted from the Avizo process.

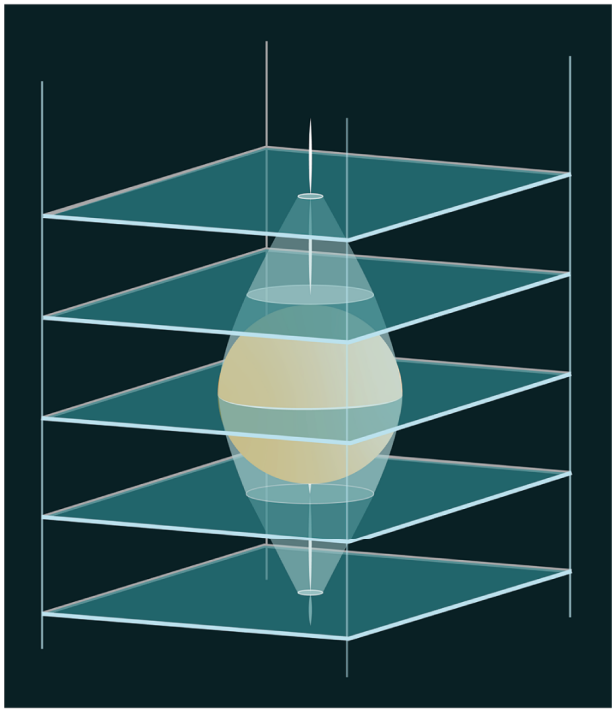

Figure 4. A representation of the fluorescence emitted from a particle in the experiments. The layers represent the image slices in the z-direction measured with the confocal microscope. There is 1.4-um separation between image slices, which is on the order of the diameter of the particles. The optics in the confocal microscope attenuate the fluorescence from the particle, showing the smaller diameter and smaller intensity in the image slices above and below the centroid of the physical particle.

Random particles were selected from centroid data on an image stack. First, the total image closest to the z-position was pulled from the stack, and a 10-um x 10-um sub-volume centered on the x-position and y-position was sub-selected from the total image. This left a smaller image with the sub-selected particle in the center (Figure 5). The process was repeated for five images above and five images below this center image. It is evident that the particle is observed

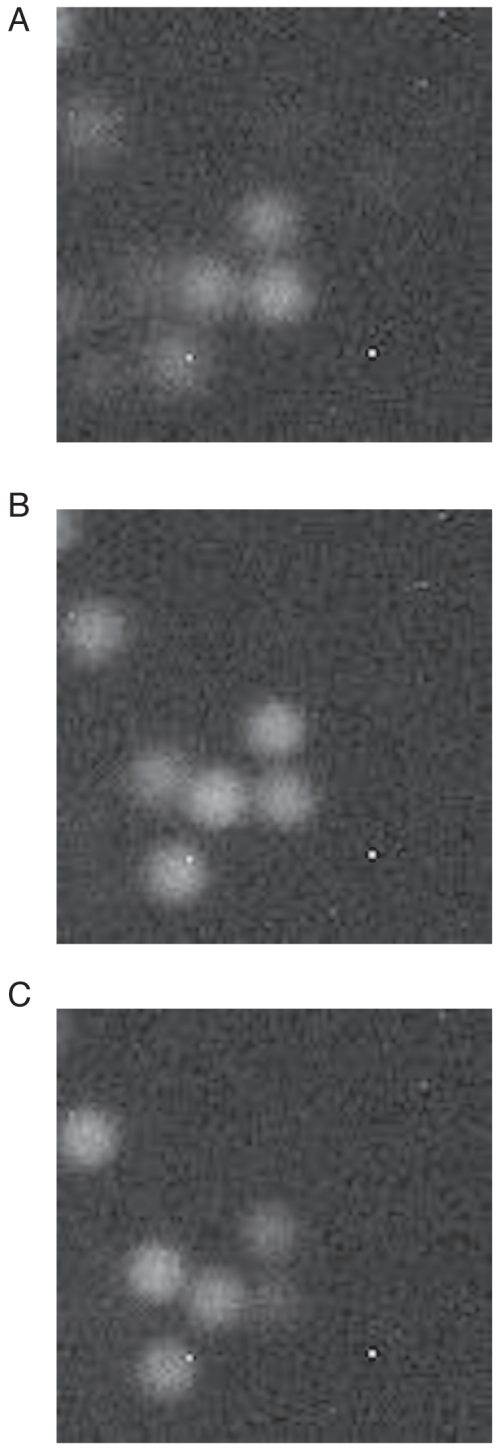

Figure 5. Three image slices pulled from an image stack adjacent to the centroid of a representative particle, where the particle is at the very center of each image. **(A)** the image slice next (no. 25) above the physical centroid. **(B)** The image slice (no. 26) closest to the centroid of the physical particle. **(C)** The image slice (no. 27) next below the centroid of the physical particle.

in multiple images—several above and below the image determined in the centroid analysis. Second, the average intensity of a 1 um x 1 um region at the center of the particle (and image) was calculated, plotted versus depth or slice number, and fitted to a Gaussian (Figure 6). The 2-um-diameter particles appear over nearly a 10-um distance in the z-direction because of the optics in the confocal scope. Finally, the z-position of this Gaussian analysis for several random particles through the depth of the science volume were compared (Figure 7), showing good agreement.

Determine of Particle Distributions in the Stack

For the computations, the science volume is parsed into volume elements into one of two ways. Rectangular volume elements are used to characterize volumes with regards to thermal gradients parallel to the direction of observation (z-direction). A rectangular volume is bound in the x-direction and y-direction by size of the image and bound in the z-direction by the image planes of each slice (Figure 8a). The first rectangular volume element is the volume between the first slice and second slice, the second rectangular volume is the volume between the second slice and third slice, and the nth rectangular volume is given by the volume between slices n and (n+1). Annulus-cylinder volume elements are bound top-and-bottom by the depth of the science volume, edge-to-edge by an inner-radius, and an outer-radius of the annulus (Figure 8b). In this work, each annulus-cylinder is in the center of the image. The first annulus-cylinder has an inner-radius of zero and outer-radius of r/10 , the second annulus-cylinder has an inner-radius of r/10 and outer-radius of 2r/10, and the nth annulus-cylinder has an inner-radius of [r·(n-1)]/10 and an outer-radius of (r·n)/10, where r is the distance from the center to the edge of the field of view in the y-direction.

Finally, often the field of view within the images show uneven light requiring some corrective compensation. A “gradient” compensation was run on each image (not per particle on each stack) by fitting a non-linear multiplier for each image. The result can be seen by measuring the volume fraction in each of the annulus-cylinder volume elements both in the rectangular and radial volumes (Figure 9). The intrinsic volume fraction was uniform over the science volume and was set by mixing and confirmed by measurement with the low magnification objectives notice that the differences in the measurement results from missing particles in the outer cylinders result from uneven illumination. This number can be used to normalize volume fraction estimates over the entire science volume but cannot be used to re-construct any connectivity.

Determining Particle Connectivity

Two particles are said to be “bonded” when the distance between centroids is 1.7 ums, or twice the radius of the

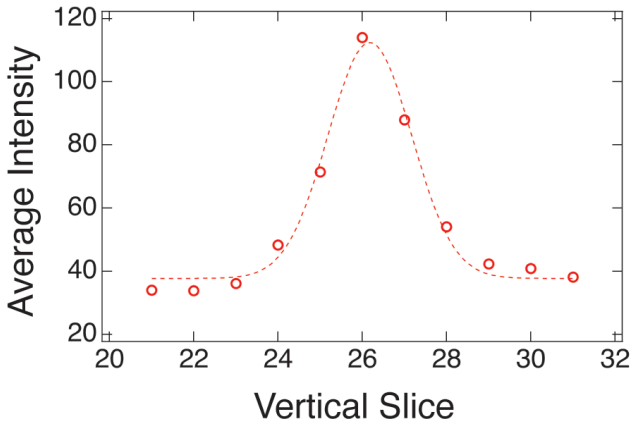

Figure 6. The average flurorescence intensity (circles) from the same representative particle (Figure 5) measure from the image slices above and below centroid of the physical particle. The data are fit to a Gaussian distribution (dashed line), where the maximum is taken as the actual centroid of the physical particle.

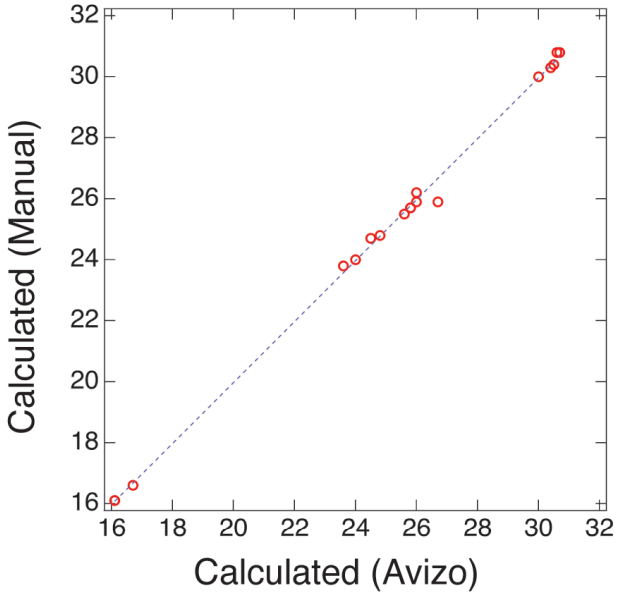

Figure 7. To ensure the fidelity of the centroids of the particles determined through the Avizo software, the z-positions of a number of particles in the image stack at different positions in the z-directly were manual determined and compared the z-positions of the same particles determined through Avizo. The correlation demonstrates good agreement.

colloidal particles. To set this distance, a pair distribution function (Egelstaff, 1967) was created from these data sets from the first image stack in each experiment (Figure 10). For each particle in the science volume, the 3D distance between this particle and every other particle in the volume binned in 0.2 um segments out to 5-um separation. The function was

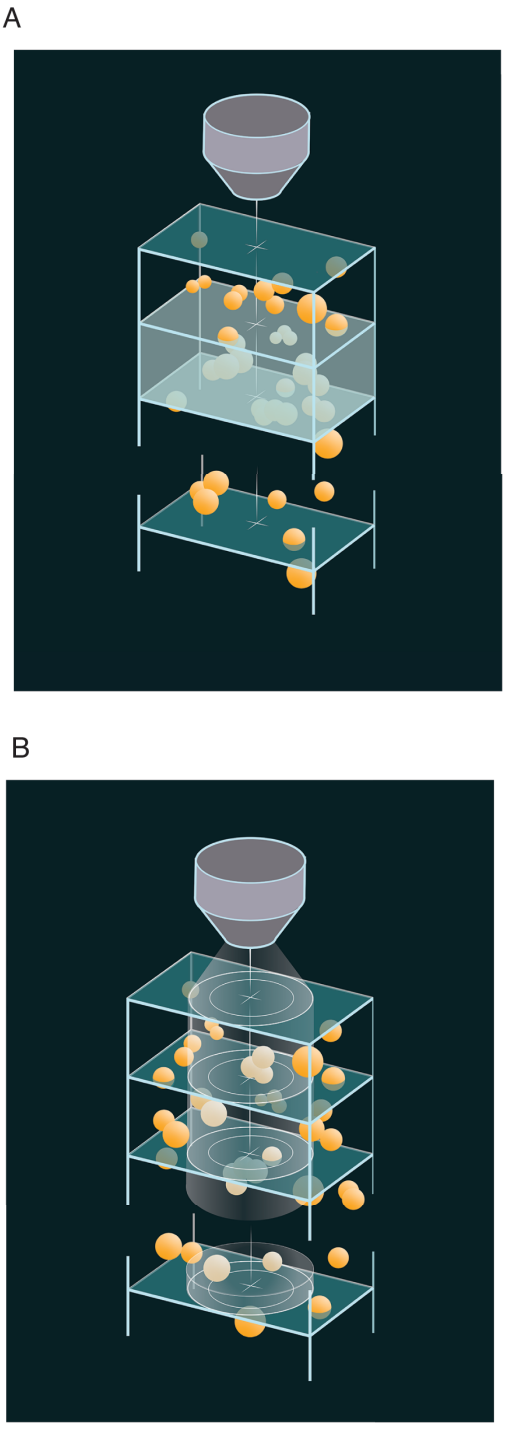

Figure 8. A representation of the two calculated volumes: vertical volume and radial volume, used in the analysis in these experiments. **(A)** The vertical volume is bound by the volume between the n and (n+1) image slices, and the x- and y-dimensions of the image. **(B)** The radial volume is bound by the volume of the cylindrical annulus of radii of (r·(n-1))/10 and (r·n)/10 through the entire dimension in the z-direction, where n is an integer between 1 and 10.

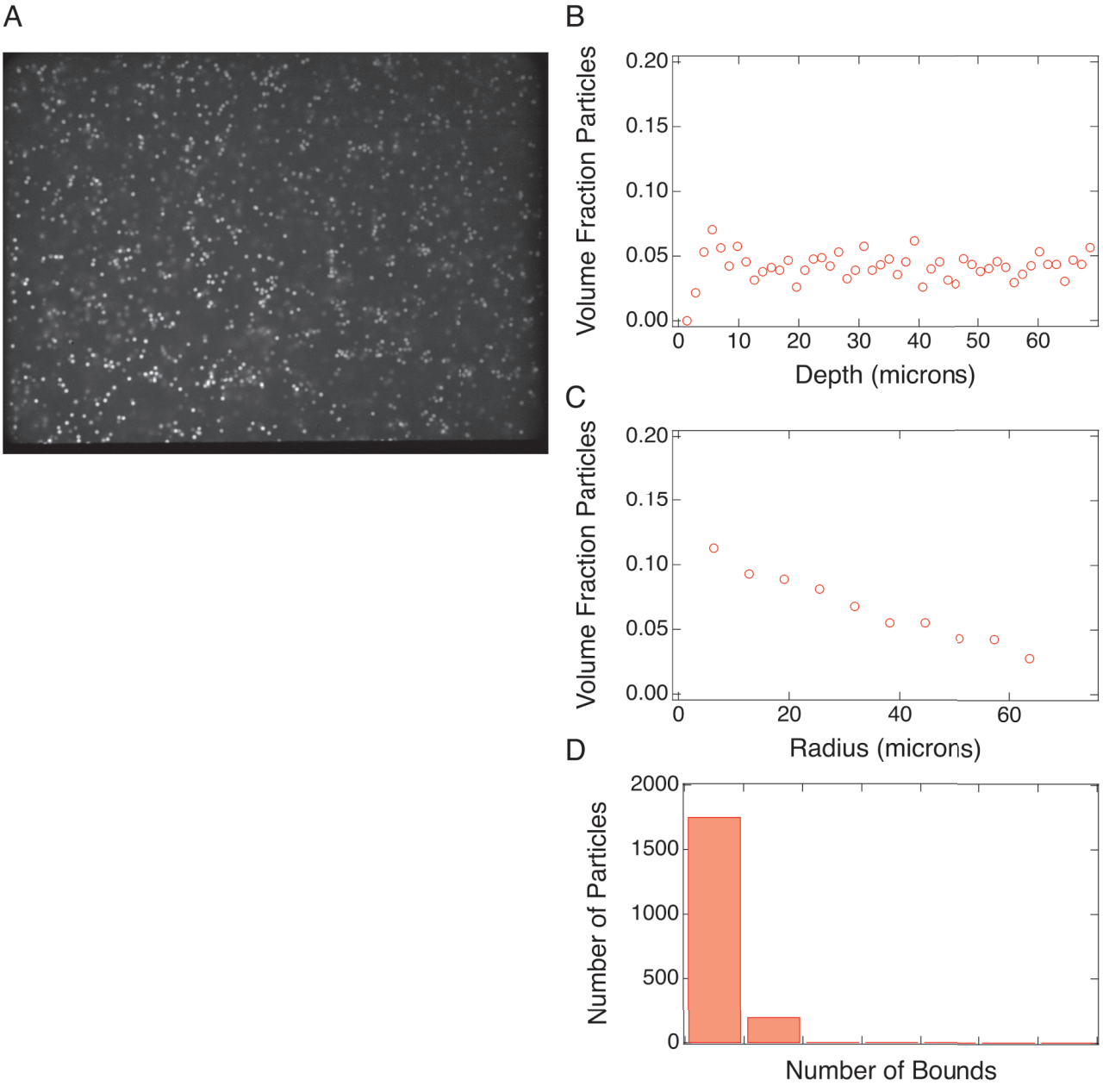

Figure 9. Data from a representative image stack. **(A**) Initial image slice with the TEM set at 20°C and at 14 um in the z-direction into the volume. **(B)** The volume fraction of particles in each vertical volume in the image stack. **(C)** The volume fraction of particles in each radial volume in the image stack, where the apparent decrease in volume fraction with increasing radius reflects the uneven lighting from the confocal microscope. **(D)** The pairwise binding between particles in the entire measured volume.

normalized by average the numbers longer than 2.5 um. There is a strong primary peak in the bin of 1.6 – 1.8 um, and 1.7 um is chosen as a representative distance associated with bonded particles. The number of bonds for each particle in the science volume: equal to zero reflect the number of unbonded particles, the number of bonds equal to one reflect the number of bonded pairs, the number of bonds equal to two reflect the number of trimers, et cetera. Significantly aggregated pieces of particles in the volume are evident from significant number of bonds in the data set.

Calculated Temperature Gradients

The temperature gradient was estimated through steady-state numerical analysis using COMSOL Multiphysics software. The

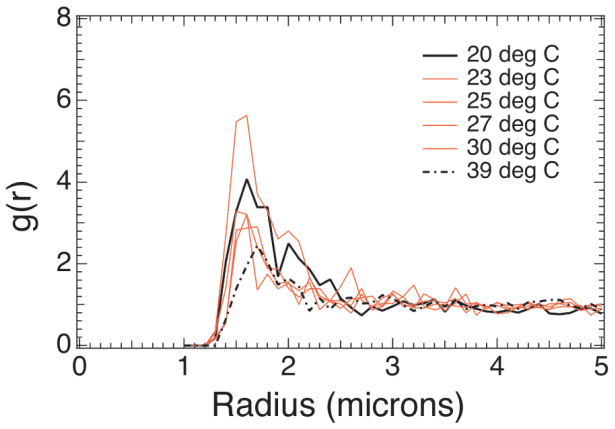

Figure 10. The probability of finding two particles at a distance – r, normalized to unity at large r, for the initial measurement when the TEM was set to different temperatures. These data show a peak at about 1.7 um reflects the separation between bound particles, and where the difference in the magnitude of the peak reflects the difference in particle volume fraction in each experiment.

dimensions and the compositions of the complete experiment were set up within the software (Figure 11). In particular, the TEMs temperature were accounted for by setting the temperature as the boundary condition on the bottom of the cell and varied between 20°C to 39°C. The objective temperature was accounted for by setting the temperature of circular spot with the diameter of the objective as the boundary condition on top of the cell and set to 28°C presumed to be a few degrees higher than the cabin temperature resulting from heating in the microscope. The cabin temperature was accounted for by setting the temperature as the boundary condition over the rest of the surface of the cell and set to 25°C, reflecting the cabin temperature on the International Space Station. All the computations were run until the model converged to the final steady-state. The temperature settings were set as close as possible to those set in the experiment. The temperature of the TEMs and the cabin were independently measured during the experiments; however, the temperature of the objective was estimated. It was presumed to be different than the cabin temperature as experiments using the non-contact objectives show no migration of particles. The direction of the migration and the nulling of the migration at about 28°C provided a good estimate of the temperature of the objective, and small adjustments to the objective temperature only resulted in proportional changes to the calculated temperature gradient. The computations show that temperature gradients in the z-direction could be large and essentially linear over the measured volume. Figure 11a shows the temperatures as seen down the x-direction (long axis) of the cell with the z-direction vertical and y-direction horizontal. The dark blue along the bottom of the cell reflects the temperature of the TEMs set at 20°C. The red along the top of the cell reflects the higher temperature from the objective set at 28°C. The yellow along the remaining faces of the cell reflects the temperature from the cabin set at 25°C. Figure 11b shows the steady-state solution for the temperature along the vertical line from the center of the objective to the bottom face of the cell. There is some temperature drop over the width of the glass of the cell. However, the temperature gradient across the solvent is essentially constant. This calculation suggests that the temperature gradient across the 200-um solvent gap can be as large as about 3.7 x 10^5 °C m^{-1} with the TEMs set to 20 °C. The steady-state solutions were calculated after changing the TEM temperature between 20°C and 31°C in 1°C steps, showing the same characteristic features in the temperature gradient. Figure 11c, shows the dependence of the temperature gradient with changing TEM temperature. Finally, the temperature gradients in the x-direction and y-direction were small owning to the much larger distances in the solvent, and experimental evidence suggests and radial motion of the particles resulting from these smaller temperature gradients are largely nulled by the Brownian force.

Results

Calibration of the Flux with Soret Force on Particles

The initial estimates for temperature settings were achieved through a series of experiments, in which for each experiment the temperature of the TEMs was fixed and flux of particles within volume of the sample was measured over time. Each experiment was initiated by mixing the sample volume with the goal of both evenly dispersing the particles through the volume and breaking up pre-formed aggregates. Sample viability—where the volume had 500–1000 unbounded dispersed particles for good statistics and devoid of obstacles such as bubbles—was confirmed with a combination of measurement with a 2.5X and 10X objectives (Figure 12). This often required translating and rotating the stirring bar through the entire length of the sample for at least 1 hour. If at the end of an hour the particles were not uniformly dispersed through the volume, the sample is remixed for another hour in the region of accumulation. The science spot was selected to be away from any obstacles and region of significant particle concentration at the ends of the cell. At this point, a drop of immersion oil was placed on the top of the cell and the 63X objective was then translated over the viable science spot. The temperature of the TEMs was set, and the sample was allowed to equilibrate for about 5 minutes. The cell was vertically positioned by finding the interface between the glass and solvent, and then translated to measure a slice 20-um into the volume. One image per minute was collected at this position over about 200 minutes. The number of particles in

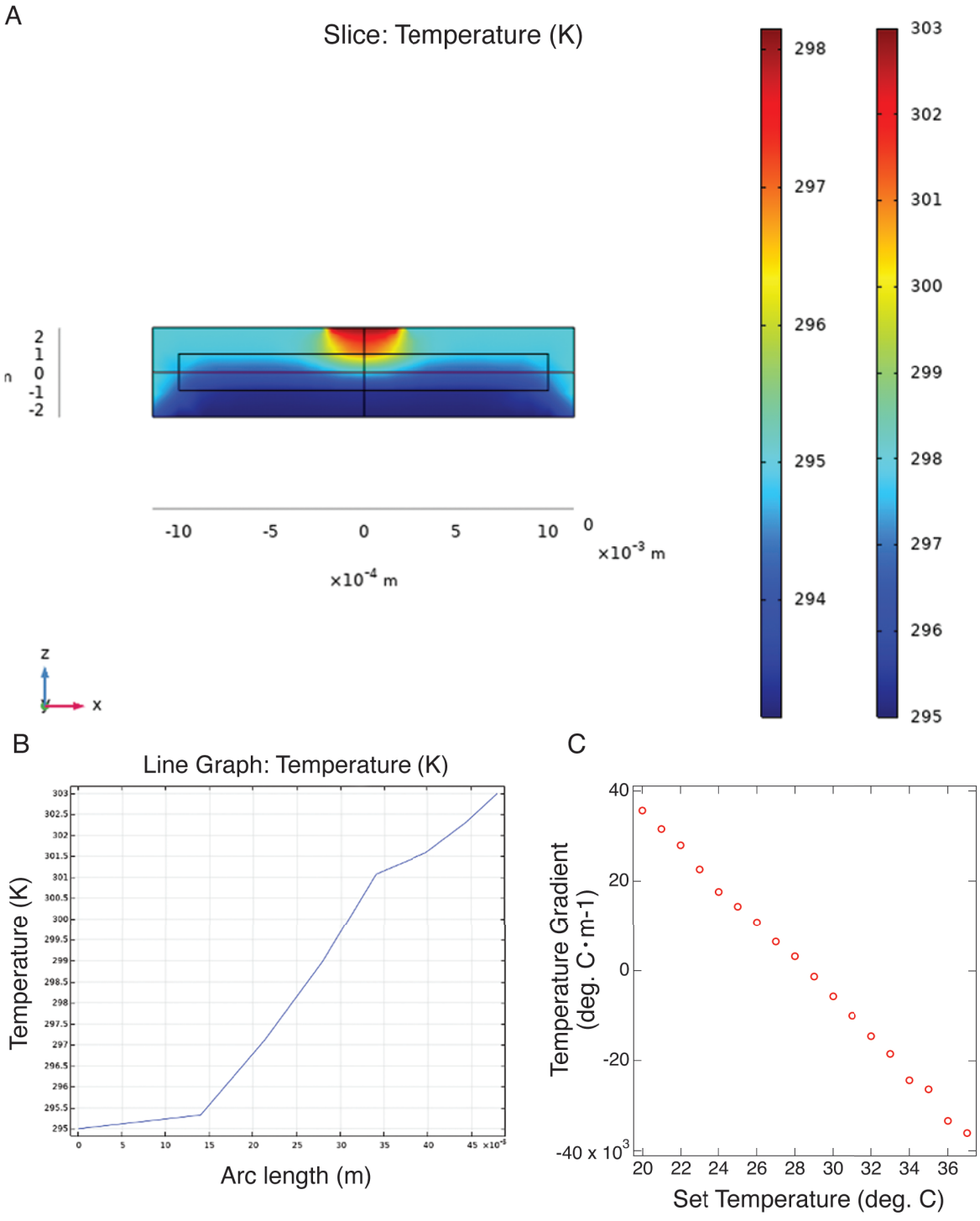

Figure 11. Modeling the temperature gradients in these experiments in COMSOL. **(A**) Temperature in the glass capillary cell looking down the x-axis. In this computation, the blue along the bottom reflects the 20°C set point of the TEM, the red along the top of the cell reflects the temperature of the objective set to 28°C, and the yellow/green along the balance of the cell reflects the temperature of the cabin at 25°C. **(B)** The computed temperature gradient across the 200-um width of the solvent in the cell from the center of the objective through the sample to the thermal bridge. The temperature drop is essentially linear through the solvent. **(C)** The temperature gradient across the solvent gap with different applied TEM temperatures, with large temperature gradient resulting from the small width of the gap.

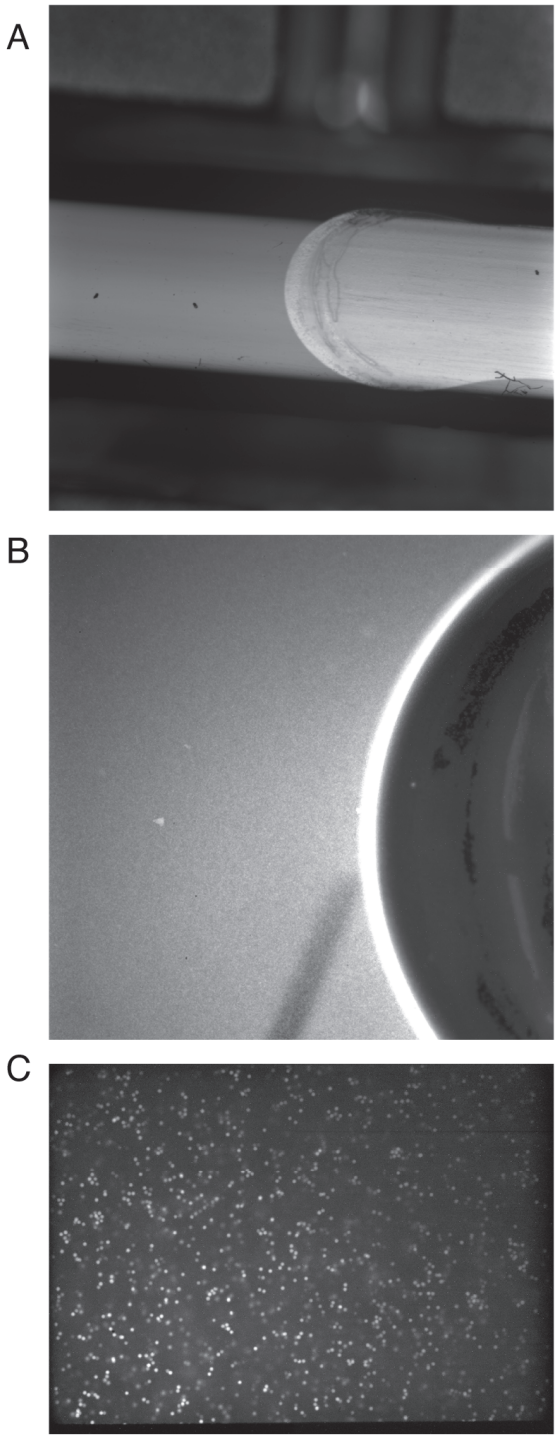

Figure 12. Typical images from these experiments. **(A)** Bright field image taken with a 2.5X air objective, showing section of the cell with sample on left and bubble on the right. **(B)** Bright field image taken with a 10X air objective, which shows graininess from the dispersed particles and shows a section of the magnetic stir bar. **(C)** Confocal image taken with 63X oil objective showing one image slice in the stack with the particles as the bright objects.

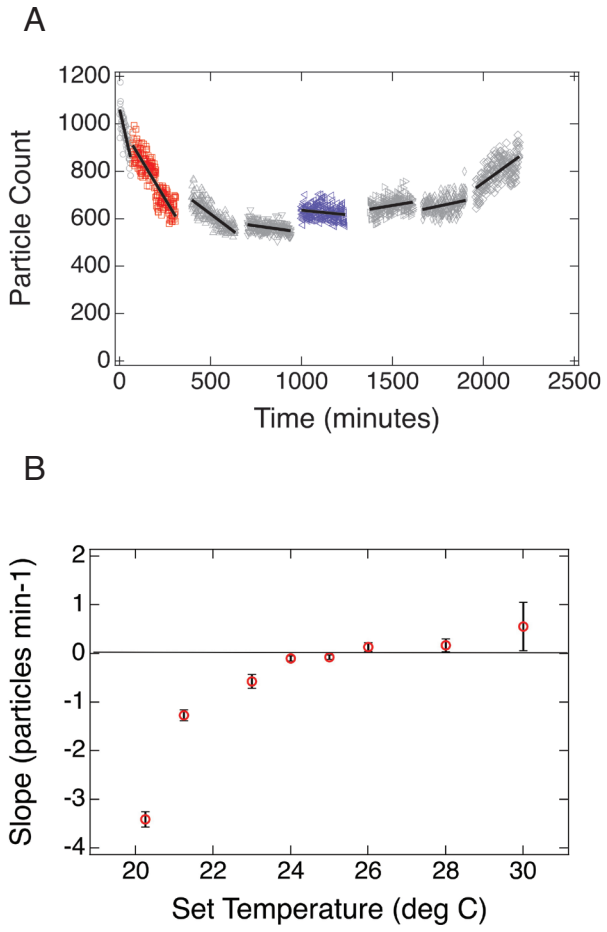

Figure 13. Initial experiments demonstrating the presence of the Soret forces. **(A).** Each set of markers represents a single experiments at different TEM temperatures: 20.0°C, 21.0°C (red), 23.0°C, 24.0 °C, 25.0 °C (blue), 26.0 °C, 28.0 °C and 30.0°C, respectively, from left to right. The particle count was measured in a volume slice at 20-um into the sample. The dark lines show the change in the particle count in the volume over time. At 20.0°C, there is large decrease in the particle count while at 30.0°C, there is a significant increase in particle count. **(B)** The change in particle count plotted versus the TEM set temperature. The change is "flattened" and nulled, between about 24°C and about 26°C.

each of the images was counted. The number of particles per image per time was plotted to measure the particle flux with the set temperature of the TEM (Figure 13a). The entire experiment was repeated at the next TEM set temperature.

It is evident that the particle flux is dependent on the temperature setting of the TEMs (Figure 13b). All the data collected at one set temperature of the TEMs was fit to line, where the slope of the line provided a mean flux expressed in the change in the number of particles per minute. When the temperature is set below about 25°C–26°C, the particles move away from the objective with increased velocity the cooler the temperature on the TEMs. When the temperature

is set above about 28°C–29°C, the particles move toward from the objective with increase velocity the hotter the temperature on the TEMs. The common observation is that the particle velocity is in the opposite direction of the temperature gradient (i.e., negative sign). The observation is consistent with those published measurements, where particles preferentially migrate to the colder surface. When the temperature set at the TEM is very large (e.g., 39°C), the particles concentrate significantly on the top surface of the cell. It is important to recall that in the absence of the objective touching the cell, there was no measured net flux of the particles with time.

Finally, there was essentially no radial net flux of the particles under these conditions. It is thought that the temperature gradients in the x-direction and the y-direction are too small resulting from the large distances to the cell edges, to drive the particles harder than Brownian forces to disperse the particles. Although the apparent radial distribution of the particles is influenced by uneven illumination over the measured volume, the relative change of each radial section can be used to confirm this statement.

Magnitude of Soret Force on Particles

The strategy for determining the magnitude of the Soret force is the reapplication sedimentation theory of Brownian particles in a gravitational field, modeling the particle distribution at long-time equilibrium and assigning the perceived gravitational force to the Soret force. The Soret force is a thermophoretic effect, originating from the differences between the interactions of solvents with the surface of the particles at different temperatures and is not a body force, such as gravity. However, the velocity of a particle resulting from the Soret force is directional and proportional to the temperature gradient: $v_s=D_t \cdot \nabla T$, where D_t is the thermophoretic mobility. The gravitational force would move an unbound particle at a constant velocity in a constant gravitational field; the temperature gradient is calculated to be constant over the width of the cell (e.g., see Figure 11), and therefore one would expect that the Soret force would also move an unbound particle at a constant velocity in a constant temperature gradient. It is reasonable to apply equivalency between the gravitational force and the Soret force. To emphasize the equivalence, measurements are made in positions in the cell of low particle volume fraction and where particles are largely unbound (e.g., see Figure 9). Finally, it should be noted that it is impractical to track individual particles, as an approach to measuring the Soret force. Considering Brownian motion alone, the diffusivity of the particles is calculated to be about $D = 8.6 \times 10^{-11}$ m^2 × s^{-1} (25°C), resulting in a mean displacement of unbounded particles of about $\Delta x \sim 125$ um (or $\Delta x/a \sim 74$) in the 30 seconds between measurement of the slices. It is impractical—if not impossible—to do individual particle tracking.

The distribution of the particles in space and time was determined from the work of Mason and Weaver (1924). In this work, the change in the number of particles at position x and at time t is determined by the one-dimension partial differential equation:

$$\frac{\partial n(x,t)}{\partial t} = A\frac{\partial^2 n(x,t)}{\partial^2 x} - B\frac{\partial n(x,t)}{\partial x}$$

Where the first term represents the flux from Brownian motion of the particles and the second term reflects the flux from motion of the particles in a gravitational field, where A is the coefficient for Brownian flux in units of m^2, and B is the coefficient for gravitational flux in units of meters. In short, the gravitational field pulls particles in the direction of the field while Brownian forces pushes particles in the opposite direction from emerging concentration gradient as the particles concentrate in one side of the volume. The equation is solved with the boundary conditions of no particle flux at the edges and with the initial concentration of the particles in set to n_o:

$$\frac{n(y,t')}{n_o} = \frac{e^{y/\alpha}}{\alpha(e^{1/\alpha}-1)}$$
$$+ 16\alpha^2\pi e^{(2y-t')/4\alpha}\sum_{m=1}^{\infty}\frac{e^{-\alpha m^2\pi^2 t'}\, m\left(1\mp e^{-1/2\alpha}\right)sin(m\pi y) + 2\pi m\alpha cos(m\pi y)}{(1+4\pi^2 m^2\alpha^2)^2}$$

The analytical solution is simplified by replacing the thickness, time, and coefficient with the following: $\alpha=A/BL$, $\beta=L/B$, $y=x/L$ and $t'=t/\beta$, where A and B are discussed above, L is the thickness of the sample in units of meters, and t is the elapsed time in units of seconds. In effect, a is the ratio of the particle flux from Brownian forces over the particle flux from the gravitational forces and is dimensionless; b is gravitational flux over the distance and has units of time; t' is the ratio of elapse time over the time of the gravitational flux and is dimensionless; y is the fractional thickness, which is zero at one end of the volume side of the objective, and L is the far end of the volume. An important aspect of the equation is that it has two parts: time-dependent part and time-independent part. At long-times, the time-dependent part converges to zero, and the equation converges to the time-independent part. The result is that $\frac{n(y,0)}{n_o}=1$ (initial distribution) and $\frac{n(y,\infty)}{n_o}=\frac{e^{y/\alpha}}{\alpha(e^{1/\alpha}-1)}$ (long-time distribution).

Experiments are done by first creating a uniform dispersion of particles in the volume and normalizing the initial distribution to unity, and by second creating a long-time distribution of the particles after applying a fixed temperature to the TEM. A sample was completely homogenized using the magnetic stirring bar. The 63X objective was placed on the top of the volume (i.e., at y = 0), and the temperature was applied to the TEMs at the bottom of the volume (i.e., at y = 1) to initiate the

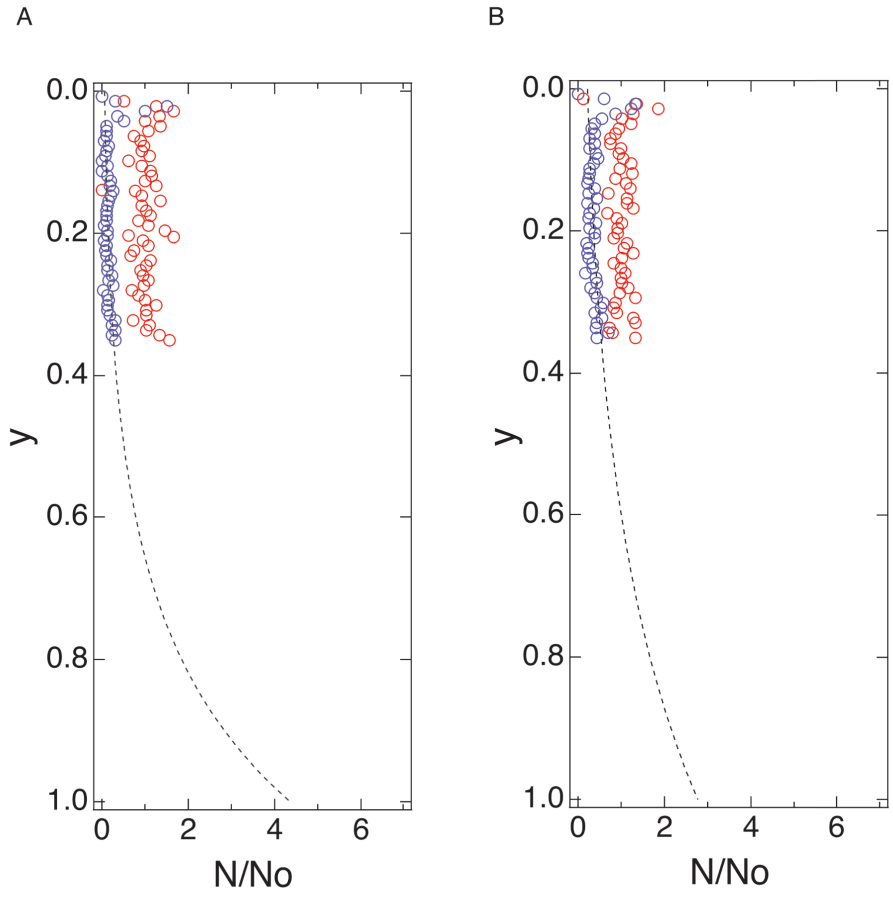

Figure 14. Sedimentation of the particles in the presence of the temperature gradient **(A)** The normalized distribution of particles at the initial condition (red); the distribution after long-time convergence when TEM set to 20°C (blue); the fit in accordance with Mason and Weaver (1924) (black dash). **(B)** (red) The normalized distribution of particles at the initial condition (red); the distribution after long-time convergence when TEM set to 23°C (blue); the fit in accordance with Mason and Weaver (1924) (black dash).

experiment. The first fifty-image-deep stack was immediately taken, measuring about 70-um of the 200-um thickness of the volume. The number of particles in the horizontal volume was determined as previously described. Each of the fifty horizontal volumes was normalized against the average number of particles over all the entire measured volume. The procedure was repeated many times. The final fifty-image-deep stack was taken after about 10,000 seconds. The data set was normalized against the initial average number of particles. This left two sets of normalized data—one initial and one at long-times—for each TEM set temperature (Figure 14) plotted in a format consistent with Mason and Weaver (1924). A value of a was numerically determined for each point of y (i.e., y = 0, y = 0.007, y = 0.014, …, y = 0.350) in the long-time data associated with each TEM temperature. The reported value is the average value of a over all the data points.

The calculation of a at each TEM set temperature is used to calculate the Soret force at each temperature. First, the Brownian flux coefficient A was calculated from $A=RT/N6\pi\mu a$, where the mean temperature is set to 25°C, m is measured at 3 x 10^{-3} Pa s, a is the particle radius taken a 0.85 x 10^{-6} m, R is the gas constant, and N is Avogadro's Number, with a value of about 7.28 x 10^{-14} m^2. Second, the value of L is known to be 2.0 x 10^{-4} m. Third, B is calculated from knowing A, a, and L. Finally, the Soret force is then calculated from the gravitational flux coefficient as $X=B\cdot 6\pi\mu a$ in Newtons. The force of gravity on the same particle on Earth would be about 2.5 x 10^{-14} N (with no buoyancy), assuming the density of the particle r = 1000 kg · m^{-3} and g = 9.8 m · s^{-2}, and expressed X is expressed in milli-G. These data for different TEM set temperatures (and different temperature gradients) are given in Table 1.

Discussion

There are several checks on these data to ensure the results are reasonable. First, the calculated force is compared to

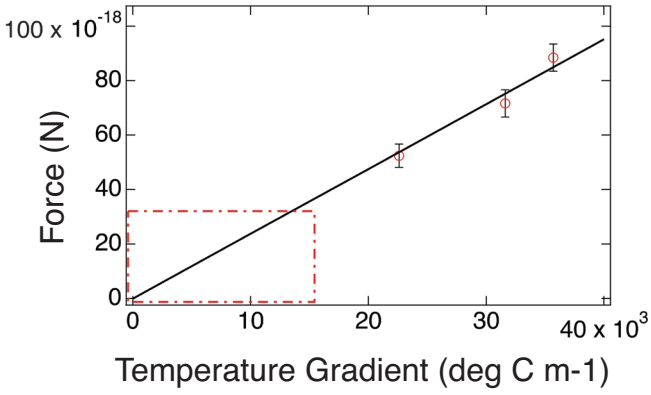

Figure 15. Force-temperature gradient curves, where force curves are determined from long-time distribution of particles and the temperature gradient determined by COMSOL modeling at three TEM set temperatures. The force is proportionally to the temperature gradient, which is internally consistent despite different approaches to generating the data. The box (dashes) represents region in which the Soret force is comparable to (or less than) the Brownian force, which results in imperceptible separation of the dispersion even with a temperature gradient (i.e., between about 24°C and about 26°C).

Table 1. Parameters for force calculations.

TEM Setting	a	A	B	Force	Force
20 °C	0.2326	7.28 x 10^{-14} m^2	1.56 x 10^{-9} m	8.85 x 10^{-17} N	3.0 milli-G
21 °C	0.2868	7.28 x 10^{-14} m^2	1.27 x 10^{-9} m	7.17 x10^{-17} N	2.7 milli-G
23 °C	0.3918	7.28 x 10^{-14} m^2	0.93 x 10^{-10} m	5.25 x 10^{-17} N	2.0 milli-G

Mason and Weaver (1924), where A reflects the thermal (Brownian) force on the particles, B reflects the gravitational force on the particles, and a is the ratio of the forces, scaled per unit length.

temperature gradients, at each TEM set temperature. These values were obtained with two independent approaches. The force is calculated (above) from the long-time distribution of particles in the volume; the temperature gradients are estimated from the COMSOL simulations and should scale proportional to the forces. In fact, a plot of the calculated temperature gradient versus the calculated force (Figure 15) shows the proportionality, which reasonably goes through (0,0).

Second, it is important to confirm that 10,000 seconds is enough time to ensure the time-dependent part of the solution goes to zero. It was already established that the Brownian motion particles is significant in distance over 30 seconds. Using the estimated Soret forces on the particle, it is also possible to determine the amount of time required to travel 200 um across the volume. The terminal velocity of the particle at 25°C is $v=F/6\pi a\gamma$, so that the time is about 100 seconds even at the largest temperature gradient (i.e., largest force). The long-time data are collected at 10,000 seconds, or more than two orders of magnitude longer than the travel time across the volume. Both checks are internally consistent with the outcomes.

Third, data from other TEM temperature settings are also instructive. At 25°C, the long-time distribution of the particles shows little change within the margin of error versus the initial particle distribution. This is consistent with Figure 13b, which shows little change in the particle count with time at this temperature. Extrapolation of the data in Table 1 suggests that the force on a particle is about 2.75 x 10^{-17} N. This gravitational force in the Mason model results in a value of a about unity, using the Brownian force at this temperature and the thickness of the volume. This means that the Brownian force is on the same order as the gravitational force (i.e., A ~ B) and that the particles remain largely uniformly dispersed at long-times. The box included on Figure 15 highlights gradients—that while non-zero, do not result in significant separation of the particles. It is suspected that this effect gives rise to the relative flat region (slope of about zero) between 24°C and 28°C in Figure 13b. This sets a practical lower limit of force of about 1 milli-G for this combination of chemistry and experiment. At 30°C (or greater), the long-time convergence of the particles concentrates in the volume adjacent to the objective. Consistent with the COMSOL computations in Figure 11c, these settings are expected to flip the sign of the temperature gradient and reverse the direction of the force. The net effect is to pull the particles toward the objective and push away from the TEM heaters.

Conclusions

The work focused on measuring the initial condition and long-term convergence of the distribution of particles in model colloidal dispersion in microgravity and modeling these distributions to determine an effective range in the magnitude of the Soret force. The magnitude of the Soret force was determined in a low-particle-density volume of the sample and tuned between about 10 x 10^{-17} N (3 milli-G) to about 3 x 10^{-17} N (1 milli-G) by adjusting the temperature gradient. The upper limit was set by the ability to set temperature on one side of the sample volume, and the lower limit was set by the dominance of Brownian forces to dominate the motion of the particles. Nonetheless, these forces enable the ability to measure changes in the colloidal systems in high-particle-density volume of the sample and map the magnitude and the ratio of forces on the properties of clumpy polymer gel systems. This work is in progress.

Acknowledgments

The authors gratefully acknowledge the following for their invaluable contributions to this effort. Drs. Gerard Baillely and Ron Swift (Procter & Gamble) for the vision, support, and encouragement to take research and development to completely new heights. Mr. Ronald Sicker (NASA) for continued support of the ACE and BCAT programs. CASIS for on-going access to resources, including astronaut time. For the crew at ZIN for the great partnership, particularly Louis Chesney and Tibor Lorik, for the seemingly endless hours on console during data collection. Dr. Frances Joan Alvarez (Procter & Gamble) for TEM images and characterization of the colloidal particles. Mr. Zachary Dragony (University of Cincinnati) for creating many of highest-quality images used in much of the publication that bring the science to life. Finally, Professor David Weitz (Harvard University) for tantalizing discussions at the white board that has inspired and brought this work into focus over many years.

Author Disclosure Statement

No competing financial interests exist.

References

Asakura S, Oosawa F (1954) On interaction between two bodies immersed in a solution of macromolecules. *Journal of Chemical Physics* **22**: 1255–1256.

Ashley GW, Henise J, Reid R, Santi DV (2013) Hydrogel drug delivery system with predictable and tunable drug release and degradation rates. *Proceedings of the National Academy of Science (PNAS)* **110**(6): 2318-2323.

Bailey AE, Poon WCK, Christianson RJ, Schofield AB, Gasser U, Prasad V, Manley S, Segre PN, Cipelletti L, Meyer WV, Doherty MP, Sankaran S, Jankovsky AL, Shiley WL, Bowen JP, Eggers JC, Kurta C, Lorik T, Pusey PN, Weitz DA (2007) Spinodal decomposition in a model colloid-polymer mixture in microgravity. *Physical Review Letters* **99**(20): 205701.

Braibanti M, Vigolo D, Piazza R (2008) Does thermophoretic mobility depend on particle size. *Physical Review Letters* **100**(10): 108303.

Cheng Z, Chaikin PM, Russel WB, Meyer WV, Zhu J, Rogers RB, Ottewill RH (2001) Phase diagram of hard spheres. *Materials and Design* **22**(7): 529–534.

Coussot P, Nguyen QD, Huynh HT, Bonn D (2002) Avalanche behavior in yield stress fluids. *Physical Review Letters* **88**(17): 175501.

Dibble CJ, Kogan M, Solomon MJ (2006) Structure and dynamics of colloidal depletion gels: coincidence of transitions and heterogeneity. *Physical Reviews E: Statistical, Nonlinear, Biological, and Soft Matter Physics* **74**: 04140.

Dickinson E (2015) Colloids in food: ingredients, structure, and stability. *Annual Review of Food Science and Technology* **6**: 211–233.

Dinsmore AD, Weitz DA (2002) Direct imaging of three-dimensional structure and topology of colloidal gels. *Journal of Physics: Condensed Matter* **14**: 7581–7597.

Dinsmore AD, Prasad V, Wong IY, Weitz DA (2006) Microscopic structure and elasticity of weakly aggregated colloidal gels. *Physical Review Letters* **96**: 185502.

Duhr S, Braun D (2006) Thermophoretic depletion follows Boltzmann distribution. *Physical Review Letters* **96**(16): 168301.

Egelstaff PA (1967) *An Introduction to the Liquid State*, London and New York: Academic Press.

Gao Y, Kim J, Helgeson ME (2015) Microdynamics and arrest of coarsening during spinodal decomposition in thermoreversible colloidal gels. *Soft Matter* **11**(32): 6360-6370.

Genovese DB, Lozano JE, Rao MA (2007) The rheology of colloidal and noncolloidal food dispersions. *Journal of Food Science* **72**(2): R11–R20.

Johnson LC, Zia RN, Moghimi E, Petekidis G (2019) Influence of structure on the linear response rheology of colloidal gels. *Journal of Rheology* **63**(4): 583–608.

Kodger TE, Guerra RE, Spräkel J (2015), Precise colloids with tunable interactions for confocal microscopy. *Scientific Reports*, **5**(14635): 1–10.

Kodger TE, Lu PJ, Wiseman GR, Weitz DA (2017) Stable, fluorescent polymethylmethacrylate particles for the long-term observation of slow colloidal dynamics. *Langmuir* **33**(25): 6382−6389.

Köhler W, Morozov KI (2016) The Soret effect in liquid mixtures—a review. *Journal of Non-Equilibrium Thermodynamics* **41**(3): 151–197.

Landrum BJ, Zia RN, Russel WB (2016) Delayed yield in colloidal gels: creep, flow, and re-entrant solid regimes. *Journal of Rheology* **60**(4): 783–807.

Lin YJ, Horner JS, Illie BP, Lynch ML, Furst EM, Wagner NJ (2020) Molecular engineering of thixotropic, sprayable fluids with yield stress using associating polysaccharides. *Journal of Colloid and Interface Science* **580**: 264–274.

Lu PJ, Zaccarelli E, Ciulla F, Schofield AB, Sciortino F, Weitz DA (2008) Gelation of particles with short-range attraction. *Nature* **453**: 499–504.

Lu PJ, Weitz DA (2013) Colloidal particles: crystals, glasses, and gels. *Annual Review of Condensed Matter Physics* **4**: 217–233.

Lynch ML, Colina CJ, Horenziak SA, Illie BP, Gizaw Y, Sun Y (2018) Phase-stable, sprayable freshening composition comprising suspended particles. Patent US 10,888,633 B2.

Lynch ML, Horenziak SA, Illie BP, Yeary AJ, Colina CJ (2020) Structured aqueous compositions having dispersed liquid benefit agent droplets. Patent Application US 2022/0226225 A1.

Manley S, Cipelletti L, Trappe V, Bailey AE, Christianson RJ, Gasser U, Prasad V, Segre PN, Doherty MP, Sankaran S, Jankovsky AL, Shiley B, Bowen J, Eggers J, Kurta C, Lorik T, Weitz DA (2004)

Limits to gelation in colloidal aggregation. *Physical Review Letters* **93**(10): 108302.

Mason M, Weaver W (1924) The settling of small particles in a fluid. *Physical Review* **23**(412): 412–426.

Ning H, Buitenhuis J, Dhont JKG, Wiegand S (2006) Thermal diffusion behavior of hard-sphere suspensions. *Journal of Chemical Physics* **125**(20): 204911.

Padmanabhan P, Zia RN (2018) Gravitational collapse of colloidal gels: non-equilibrium phase separation driven by osmotic pressure. *Soft Matter* **14**(17): 3265–3287.

Platten JK (2006) The Soret Effect: a Review of Recent Experimental Results. *Journal of Applied Mechanics* **73**: 5–15.

Putnam SA, Cahill DG (2005) Transport of nanoscale latex spheres in a temperature gradient. *Langmuir* **21**(12): 5317–5323.

Putnam SA, Cahill DG, Wong GCL (2007) Temperature dependence of thermodiffusion in aqueous suspensions of charged nanoparticles. *Langmuir* **23**(18): 9221–9228.

Rueb CJ, Zukoski CF (1997) Viscoelastic properties of colloidal gels. *Journal of Rheology* **41**(2): 197–218.

Russel WB, Saville DA, Showalter WR (1999) *Colloidal Dispersions*, Cambridge University Press.

Sabin J, Bailey AE, Espinosa G, Frisken BJ (2012) Crystal-arrested phase separation. Physical *Review Letters* **109**(19): 195701.

Solomon MJ, Spicer PT (2010) Microstructural regimes of colloidal rod suspensions, gels, and glasses. *Soft Matter* **6**: 1391–1400.

Suman K, Wagner NJ (2022) Anomalous rheological aging of a model thermoreversible colloidal gel following a thermal quench. *Journal of Chemical Physics* **157**(2): 024901.

Swan JW, Vasquez PA, Whitson PA, Fincke EM, Wakata K, Magnus SH, De Winne F, Barratt MR, Agui JH, Green RD, Hall NR, Bohman DY, Bunnell CT, Gast AP, Furst EM (2012) Multi-scale kinetics of a field-directed colloidal phase transition. Proceedings of the National Academy of Science (PNAS) **109**(40): 16023–16028.

Swan JW, Vasquez PA, Furst EM (2014) Buckling instability of self-assembled colloidal columns. *Physical Review Letters* **113**(13): 138301.

Van Vaerenbergh S, Legros JC (1998) Soret coefficients of organic solutions measured in the microgravity SCM experiment and by the flow and Benard cells. *Journal of Physical Chemistry B* **102**(22): 4426–4431.

Veen SJ, Antoniuk O, Weber B, Potenza MAC, Mazzoni S, Schall P, Wegdam GH (2012) Colloidal aggregation in microgravity by critical Casimir forces. *Physical Review Letters* **109**(24): 248302.

Vigolo D, Brambilla G, Piazza R (2007) Thermophoresis of microemulsion droplets: size dependence of the Soret effect. *Physical Reviews E: Statistical, Nonlinear, Biological, and Soft Matter Physics* **75**(4): 040401.

Wagner NJ, Brady JF (2009) Shear thickening in colloidal dispersions. *Physics Today* **62**(10): 27–32.

Zhu J, Li M, Rogers R, Meyer WV, Ottewill RH, STS-73 Space Shuttle Crew, Russel WB, Chaikin PM (1997) Crystallization of hard-sphere colloids in microgravity. *Nature* **387**(6636): 883–885.